Auxiliary Management and Control Channel (AMCC) for Coherent Frequency-Division-Multiplexing (FDM) PON

Jiaye Wang, Wangwei Shen, Jiang Chen, Guoqiang Li, Sizhe Xing, Nan Chi, *Senior Member, IEEE*, and Junwen Zhang

***Abstract*—The auxiliary management and control channel (AMCC) is an extra channel transmitting control and management signal to not change the GPON frame and reduce the PON system latency. In this paper, we demonstrate AMCC for control information transmission in a coherent frequency division multiplexing passive optical network (FDM-PON). In our work, we introduce the multiplication scheme of digital AMCC signal superimposition theoretically and show that the multiplication scheme can maintain a high signal-to-noise ratio (SNR) for the main signal. Thus, we apply the multiplication scheme for the AMCC signal superimposed to the coherent FDM-PON. In addition, we propose a novel extraction algorithm without interference cancellation to detect the AMCC signal. A 4-band coherent FDM-PON system with a total data rate of 100 Gbps and a 24 Mbps non-return-to-zero (NRZ) signal is demonstrated both through simulation and experiment.**

***Index Terms*—Coherent frequency division multiplexing passive optical network (FDM-PON), auxiliary management and control channel (AMCC).**

I. Introduction

With the global deployment of the fifth-generation (5G) mobile communication network, the passive optical network (PON) with higher data transmission rates, wider coverage and lower latency has been studied to meet the requirements of new services such as cloud services, virtual reality (VR) applications and edge computing [1]. However, traditional PONs based on intensity modulation and direct detection (IM/DD) in the physical layer struggle to meet the rapidly growing demand due to issues such as challenging fiber dispersion processing, low sensitivity, limited modulation dimension, and complex channel selection [2]. Therefore, coherent PON is considered as a more advantageous candidate [3]. The coherent PONs can achieve linear conversion of the optical field and modulate/detect the amplitude, phase, and polarization of the optical signal [4]. Firstly, standard dual-polarization coherent receivers are used to detect local oscillator (LO) signals with high receiver sensitivity in coherent PONs, enabling a sufficient power budget with moderate transmit power [5]. The increased sensitivity in coherent PONs is achieved by purely amplifying the signal using LO power, as opposed to IM/DD systems. The additional power budget can expand the coverage range and/or support more connected users. Secondly, while the C-band offers the least transmission loss, C-band signals are prone to dispersion, which can be challenging to compensate for in an IM/DD system. Coherent PON systems can alleviate the dispersion problem through the use of digital signal processing (DSP) algorithms [6]. Moreover, in coherent PONs, the use of higher-order modulation formats with lower transceiver component bandwidths is allowed by utilizing the four degrees of freedom of data transmission (in-phase and quadrature modes in both x-y polarization states) [7].

In the traditional time-division multiplexing passive optical network (TDM-PON), the discovery and registration process between the optical line terminal (OLT) and optical network unit (ONU) is achieved through the exchange of multi-point control protocol (MPCP) messages [8]. The registration process in traditional TDM-PON requires a quiet window, which will increase the overall latency. However, high-speed coherent PONs demand strictly low latency in 5G [9]. In order to solve the latency problem caused by the quiet window in TDM-PON, wavelength-division multiplexing passive optical network (WDM-PON) is the most favored candidate for 5G mobile fronthaul [10]. Coherent frequency-division multiplexing passive optical network (FDM-PON) is a similar scheme which is frequency multiplexing based on several subcarriers [11]. Coherent FDM-PON allows the adjustment of processing capacity and minimizes the required bandwidth at the ONU side, while still maintaining a large aggregated throughput per wavelength to save spectral occupancy. In coherent FDM-PON, all traffic flows are transmitted in parallel on different subcarriers. Several subcarriers can be grouped per wavelength into a subchannel with different modulation/coding formats, and the data rate of each subcarrier can be utilized, resulting in high subcarrier utilization [12], [13].

In WDM-PON, there is no channel to transmit the control signal. In the point to point (PtP) WDM-PON part of next

Manuscript received 30 January 2024; revised 19 March 2024; accepted 21 March 2024. Date of publication 26 March 2024; date of current version 2 May 2024. This work was supported in part by the National Key Research and Development Program of China under Grant 2023YFB2905700, in part by the National Natural Science Foundation of China under Grant 62171137, Grant 62235005, and Grant 61925104, and in part by the Natural Science Foundation of Shanghai under Grant 21ZR1408700. *(Corresponding author: Junwen Zhang.)*

The authors are with the Key Laboratory for Information Science of Electromagnetic Waves, Department of Communication Science and Engineering, Fudan University, Shanghai 200433, China (e-mail: 21210720227@m.fudan.edu.cn; wwshen21@m.fudan.edu.cn; 20210720083@fudan.edu.cn; 19210720066@fudan.edu.cn; szxing21@m.fudan.edu.cn; nanchi@fudan.edu.cn; junwenzhang@fudan.edu.cn).

Digital Object Identifier 10.1109/JPHOT.2024.3381867

generation (NG)-PON2, an additional control channel called auxiliary management and control channel (AMCC) is needed to convey wavelength assignment and allocation information and operation administration and maintenance data, enabling flexible and low-latency network management. AMCC is one of the transportation options for the physical layer operation, administration and maintenance channel [14], which is a message-based operation and management channel between OLT and ONUs that supports the PON transmission convergence layer management functions [15]. The AMCC signal is added to each individual wavelength in both, downstream and upstream with the low-speed non-return-to-zero (NRZ) signal. For the case that the WDM-PON system has to transparently transport a payload bitstream, without terminating any part of its frame structure, the AMCC signal has to be superimposed to the main signal at the same wavelength with only minor interference of the AMCC and the payload data. And the embedded communication protocol is standardized in the ITU-T G.989 series [16]. A number of previous studies have confirmed the feasibility of AMCC in WDM-PON. For example, AMCC is used to achieve wavelength control in WDM-PON systems [17], [18], [19], [20], [21]; an AMCC-managed WDM-PON system is proposed for ONU activation, wavelength adjustment, and monitoring in [22], [23]; and AMCC can be used to reduce the power penalty [24]. In addition to exploring the application scenarios of AMCC, the generation and extraction of AMCC signal is also an interesting research topic. In [25], AMCC signal is realized by controlling the DC bias of the Mach-Zehnder Modulator (MZM) to add the NRZ signal to the main signal of WDM-PON. Moreover, an algorithm that reconstructs PON by analyzing the nonlinear modulation characteristics, eliminating interference between AMCC and the main signal is proposed at the receiver side. [26] provides another method for AMCC signal generation by using a semiconductor optical amplifier (SOA) to control the amplitude of the main signal of WDM-PON and utilizes a 3-step moving averaging method based on the DSP block to extract the AMCC signal from the superimposed signal. The two methods above are realized by operating on hardware, such as MZM and SOA. Referring to control information transmission in coherent FDM-PONs, we believe that AMCC can be a candidate for the requirement of low latency [27]. However, to our knowledge, no experiments have yet demonstrated the feasibility of AMCC in coherent FDM-PON. In coherent FDM-PON, AMCC can transmit control information simultaneously with the data channel without additional bandwidth resource, enabling flexible and low-latency network management. Moreover, due to the lower bandwidth of AMCC, which makes a low impact on the data channel.

To further solve this problem, recently we proposed applying the AMCC to the coherent FDM-PON system by periodically adjusting the amplitude of the main coherent FDM-PON signal in the transmitter-end DSP and demonstrated a 4-band coherent FDM QPSK PON with the NRZ-AMCC signal. This paper is an extension of the previous report in OECC 2023 and some of the results have been presented during the conference [28]. Here we further discuss details of the configuration, the principle of the superimposition scheme of AMCC and the main signal, and key DSP functions of the AMCC signal including absolute rectification, time-domain waveforms smoothing, and energy detection. We add a VPIphotonics Design Suite simulation system to validate the feasibility of the coherent FDM-PON system, conduct a thorough analysis of the implementation of AMCC bandwidths at both 100 kbps and 200 kbps and analyze the performance results of the main signal and AMCC signal in the simulation system. Additional experimental results on larger modulation index (MI) [26] are added in this paper. As we have demonstrated in [28], the efficiency of the AMCC in coherent FDM-PON and the overall performances under different test conditions are verified, and the performance is improved by applying the novel superimposition scheme and extraction algorithm. As a proof-of-concept, we have achieved a 4-band 100 Gbps coherent FDM QPSK PON system with a 24 Mbps NRZ-AMCC signal and analyzed the system performance at different MI in the simulation and experimental demonstration.

II. Principles

Coherent FDM-PON can be implemented using Nyquist digital subcarrier modulation (SCM) techniques. Through this modulation, coherent FDM-PON allocates a unique frequency to each user on a single wavelength, allowing it to conserve wavelength resources and meet the requirement of high-capacity networks.

The schematics of the coherent FDM-PON with AMCC is shown in Fig. 1. Only one wavelength is used in the FDM-PON architecture. In the downstream, OLT broadcasts the same signals to 4 ONUs. Each ONU obtains the corresponding sub-band signal through frequency shifting and matched filtering. The main information for each user is modulated into the corresponding subcarrier. Then the main signal is loaded with the AMCC signal by adjusting the amplitude of the main signal. In other words, the AMCC signal is loaded onto the main signal by multiplication. The superimposed signal is represented as:

$$s(t) = \sum_{k=0}^{3} x_k(t) y_k(t) e^{j2\pi f_k t}, \tag{1}$$

where $x_k(t)$ and $y_k(t)$ are the main signal and AMCC signal, respectively, and f_k is the center frequency of kth sub-band. In this paper, the center frequencies of 4 sub-bands are -15 GHz, -5 GHz, 5 GHz and 15 GHz, respectively. $y_k(t)$ is expressed as:

$$y_k(t) = \sum_{m} b_k^m \Pi(t - mT_{\mathrm{AMCC}}), \tag{2}$$

where T_{AMCC} is the AMCC signal period, $\Pi(t)$ represents the rectangular shaping pulse and b_k^m is the AMCC symbol.

$$b_k^m = \begin{cases} 1, \mathrm{bit}'1' \\ 1-\alpha, \mathrm{bit}'0', \end{cases} \tag{3}$$

where $\alpha \in (0, 1)$ is the amplitude modulation index (AMI). As AMI increases, the main signal SNR decreases but the AMCC SNR increases. The SNR of the superimposed signal in this case decreased to:

$$SNR = \frac{P_s/2 + (1-\alpha)^2 P_s \Big/ 2}{P_N}, \tag{4}$$

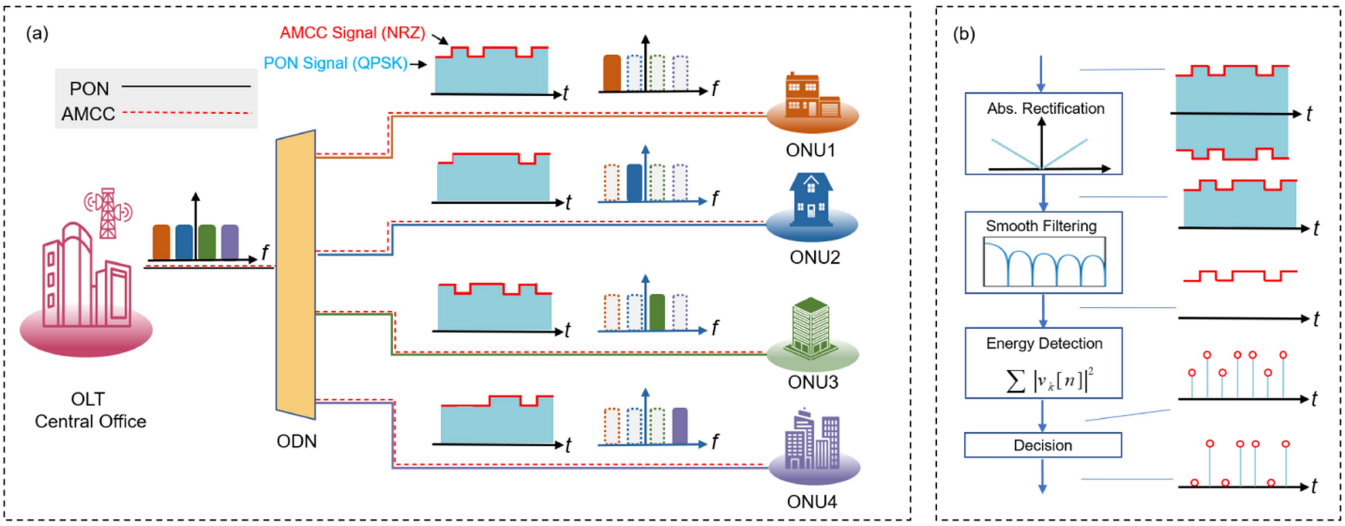

Fig. 1. (a) Architecture diagram of FDM-PON with AMCC. (b) The Rx DSP of the AMCC signal.

where P_s is the power of the original main signal without AMCC, P_N is the power of the noise. The power of the superimposed signal decreases because the peak power of the system is limited.

MI is denoted in (5). As MI increases, the amplitude of the AMCC signal grows, leading to a higher SNR for the AMCC. Meanwhile, the SNR of the main signal decreases. MI should be set to a compromise value where the AMCC signal can be demodulated without significantly affecting the SNR of the main signal.

$$MI[\%] = \frac{P_{\max} - P_{\min}}{P_{ave}} \times 100, \tag{5}$$

where $P_{\min}$, $P_{\max}$ and P_{ave} referring to the maximum, minimum and average power values of the envelope of the overmodulated PtP signal [26].

In Fig. 1, the AMCC signal is used to transmit management and control information between the OLT and the ONU in both the upstream and downstream. This enables efficient utilization of the available bandwidth in the network, allowing multiple ONUs to simultaneously transmit and receive data over a single fiber using different frequencies and providing low latency transmission. Compared with the main signal of a high data rate, the AMCC signal is a narrow-band NRZ signal of a quite low data rate. Note that the AMCC signal is generated for each user (sub-band) separately.

At the receiver end, after re-sampling and down-conversion, we process the received signal in two separate branches, i.e., the AMCC signal DSP and the main data DSP. At the branch of AMCC signal DSP, we first take the absolute value of the receiver signal to get the rectification signal. The rectification AMCC signal after taking the absolute value is represented as:

$$u_k[n] = |r_k[n]| \tag{6}$$

where $r_k[n]$ is the AMCC signal of k subcarrier after re-sampling and down-conversion.

After absolute-value rectification, the signal is filtered by a smooth filter. The AMCC signal after the smooth filter is:

$$v_k[n] = u_k[n] \otimes h[n] \tag{7}$$

where $h[n] = \frac{1}{N}, n \in \{0, 1, \ldots, N-1\}$ is the formulate of the smooth filter, $\otimes$ is the discrete-time convolution operation.

Then we calculate the energy of each NRZ symbol period:

$$w_k[m] = \sum_{n=mN_T+1}^{(m+1)N_T} |v_k[n]|^2 \tag{8}$$

where N_T represent the number of sampling points for one symbol period of AMCC signal.

At last, the discrete points after energy detection are decided as NRZ symbols:

$$a_k[m] = \begin{cases} 0, w_k[m] < E_d \\ 1, w_k[m] \geq E_d \end{cases} \tag{9}$$

where E_d is the decision threshold energy of the signal.

By using the multiplication method to superimpose AMCC onto the main signal, the main signal does not need to be eliminated during the demodulation of the AMCC signal. This means that the demodulation of the AMCC signal and the demodulation of the main signal can be done in two independent branches.

III. Numerical Setup and Results

Initially, the coherent FDM-PON system is numerically simulated to verify the rationality of the system. In the simulation, we investigate the effects of different received optical power (ROP) and MI on the performance of the main signal and NRZ signal, respectively.

A. System Model Setup

The simulation setup for the 100 Gbps 4-band coherent FDM QPSK PON system superimposed with 100 kbps AMCC signal is shown in Fig. 2. We simulate the system in commercial optical

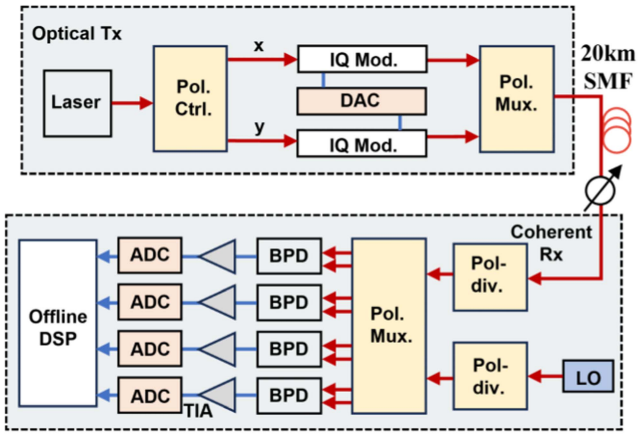

Fig. 2. Simulation setup of 100Gbps coherent FDM PON system.

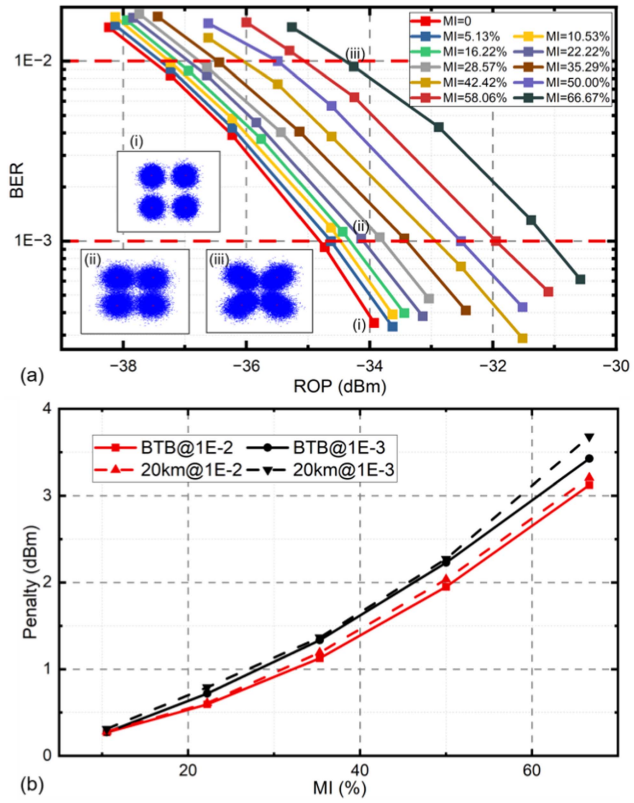

Fig. 3. The QPSK signal results of (a) BER versus ROP under 20-km SMF transmission; (b) penalty versus MI.

simulation software VPIphotonics Design Suite. The parameters of the simulation are summarized in Table I. To explore bits of NRZ signal to ensure the AMCC symbol rate of 100 kbps and ensure the allowable number of symbols of the simulation system, we select 1048576 number of symbols. In the DSP for generating the AMCC signal, we selected a 16 bits NRZ signal. The choice of the number of symbols will impact the processing speed of the simulation system, and with the selected number of symbols, the system takes more than half an hour to complete each run. On the transmission side, the generated continuous-wave (CW) lightwave with 14 dBm optical power is generated by a laser.

TABLE I
PARAMETERS OF THE SIMULATION

Simulation	Values
Number of Symbols	1048576
Laser linewidth	0.1 MHz
Laser average power	14 dBm
Laser wavelength	1550 nm
MZM VPI	4 V
Attenuation	[28 dB,32 dB]
Fiber length	20-km
PIN responsivity	1 A/W
PIN thermal noise	10^{-12} A/Hz^(1/2)
TIA input noise	7.9^{-6} A/Hz^(1/2)
TIA transimpedance	1000 Ω
ADC resolution	8 bit

Then the generated CW lightwave is sent to the polarization controller and divided into two polarizations, x-polarization and y-polarization. The CW lightwave after polarization splitting passes through the I/Q modulations which are driven by a 6.25 GBand polarization division multiplexed (PMD)-QPSK signal to conduct the I/Q modulate. The optical signal transmits through 20-km fiber after the polarization combination. On the receiver side, the optical signal after fiber transmission is sent to the variable optical attenuator (VOA) to adjust the ROP. The LO lightwave with the same optical power as the transmission CW lightwave is generated by another laser. The received optical signal and LO are divided into two polarizations separately before passing through the optical hybrid which generates four optical signals with a 90-degree angle phase difference. Then the optical signals are detected by four balanced photodiodes (BPDs) with 1 A/W responsivity. After BPD detection, the electrical signals are amplified by transimpedance amplifier (TIA) with 1000 ohms transimpedance. Finally, the signals are sampled by four analog-to-digital converters (ADCs) with an 8 bits resolution, and then conduct the offline DSP. In this simulation system, the transmission QPSK signal is generated by mapping the original signal, upsampling 16-time and I/Q separation [29]. For receiver offline DSP, splitting the main signal and NRZ signal is performed after re-sampling and down-conversion. For the NRZ signal, take the absolute rectification before passing through a smooth filter. Then calculate the energy of each signal period for further signal decision. For the main signal, chromatic dispersion compensation (CDC) is conducted before fast square-timing-recovery algorithm-based clock recovery [30]. Then, the constant modulus algorithm (CMA) based on the 25-tap T/2-spaced is performed to recover the multi-modulus and demultiplex polarization of the retiming signal [31]. After CMA, frequency offset estimation (FOE) and carrier phase estimation (CPE) are carried out to recover the frequency and phase [32]. Finally, the recovery signal is sent to QAM demodulation and bit-error-ratio (BER) calculation after T-spaced decision-directed least-mean-square (DD-LMS) equalization [33].

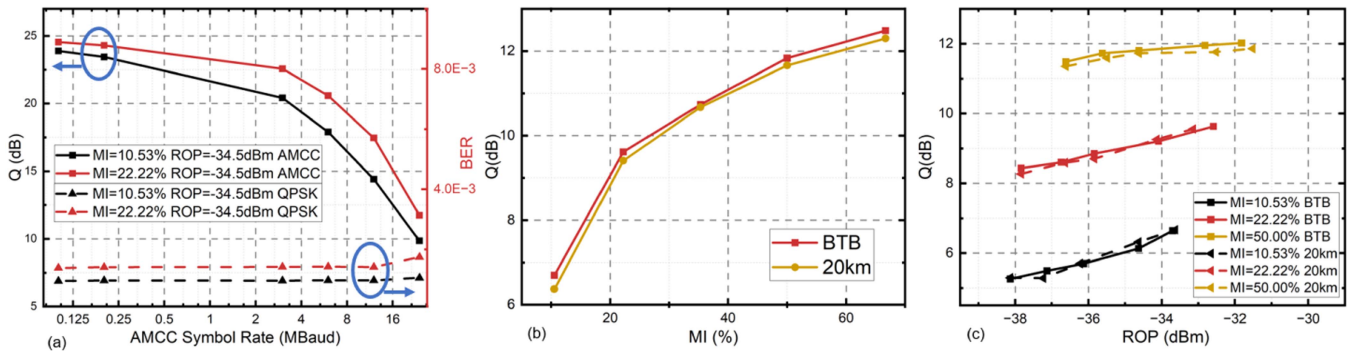

Fig. 4. AMCC signal results of (a) the Q versus AMCC symbol rate; (b) the Q versus MI; (c) the Q versus ROP.

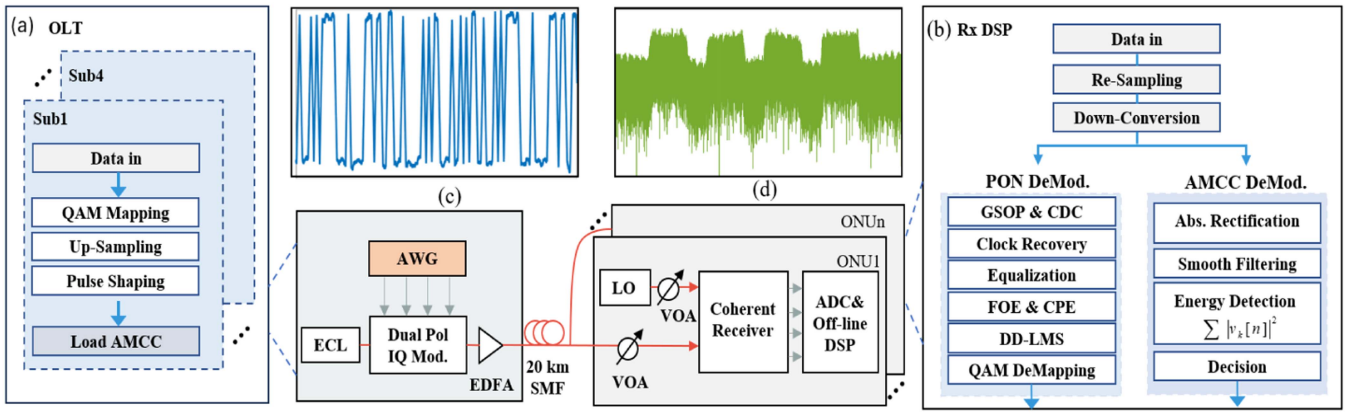

Fig. 5. Experimental setup for coherent FDM PON with AMCC. (a) and (b) are the Tx and Rx DSP; (c) the waveform diagram in the time domain; (d) the spectrum of the 4-band FDM-PON signal.

B. Simulation Results

First, the performance of the main signal with different MI and ROP is studied in the simulation. The BER versus ROP of the main signal under 20-km single-mode fiber (SMF) with different MI is shown in Fig. 3(a). In the simulation, the LO optical power level is fixed at 14 dBm. The ROP is adjusted by VOA to get the BER threshold of 1E-2 and 1E-3. In all the tests, as the MI increases the ROP of the main increases. The sensitivity of the signal is the minimum optical power received when the BER reaches the threshold of 1E-2 or 1E-3. The ROP is about −37.5 dBm and −34.8 dBm when MI is 5.13% at the threshold of 1E-2 and 1E-3 respectively. When the MI is 66.67%, the ROP increases to −34.4 dBm and −31.1 dBm at the threshold of 1E-2 and 1E-3 respectively. (i), (ii), (iii) in Fig. 3(a) are constellation charts of the main signal with 0, 22.22% and 50.00% MI under 20-km SMF. In addition, the penalty is larger with MI increasing. Fig. 3(b) shows the penalty of the main signal versus the MI. From the figure, we notice that the penalty under 20-km SMF transmission is slightly higher than that under back-to-back (BTB) fixing the specified BER threshold.

The value of Q can represent the performance of the AMCC signal. As the value of Q increases, the performance is much better. In the simulation, we test the value of Q versus AMCC symbol rate, as shown in Fig. 4(a). We conduct a study on the Q values in a lower AMCC data rate, considering both 100 kbps and 200 kbps data rate. In the simulation system, we set the number of symbols to 1048576, with 16 bits for OOK signals under a 100 kbps AMCC data rate. It is noteworthy that each measurement for a point in the Fig. 4(a) in the simulation system takes more than half an hour to complete. Fixing the MI value and ROP, the performance of the AMCC signal becomes worse with the AMCC symbol rate increasing. In addition, we find that the performance of QPSK signal changes very little when the AMCC symbol rate increases. However, it is obvious that under 100 kbps or 200 kbps AMCC symbol rate the performance of QPSK signal is better than that under 24 Mbps AMCC symbol rate. And the BER of the QPSK signal with 22.22% MI is slightly higher than that with 10.53% MI. The Q versus MI and ROP under different conditions is shown in Fig. 4(b) and (c). We discover that when ROP is −36 dBm and the symbol rate is 24 Mbps, the value of Q is larger as the MI increases. And in Fig. 4(c), as the value of ROP is larger, the performance of AMCC becomes better which is the same as that of the main signal.

IV. Experimental Setup

In order to prove the feasibility of the algorithm, an experimental design is carried out. The experimental setup for coherent FDM-PON with AMCC is shown in Fig. 5. Due to limited experimental conditions at present, we use an ONU

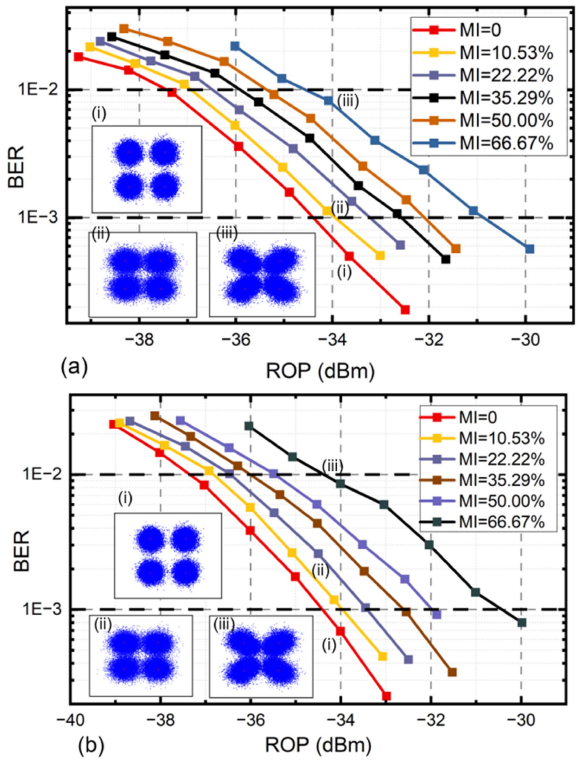

Fig. 6. QPSK signal results of (a) BER versus ROP in the BTB case; (b) BER versus ROP in the 20-km case.

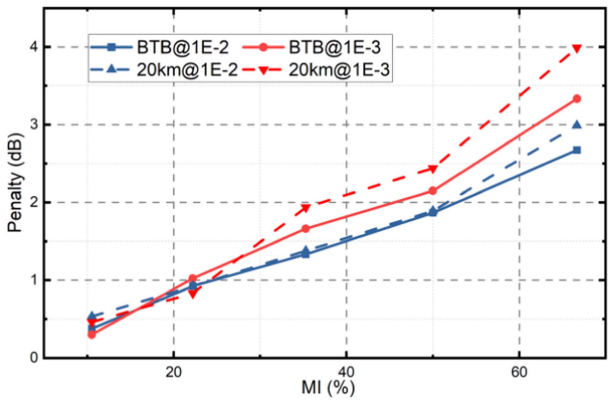

Fig. 7. QPSK signal results of the penalty of the QPSK signal versus MI.

to conceptually validate our scheme. In future work, we will provide experimental demonstrations of multiple ONUs. We use a 4-subcarrier coherent FDM-PON with each subcarrier carrying 6.25 Gbps QPSK signal and 24 Mbps NRZ signal. As the AMCC signal bandwidth increases, the BER of AMCC will increase. 24 Mbps is the maximum baud rate of AMCC for error-free in the case of 10% MI. Due to the limited length of experimental sampling data and the high transmission rate of the main signal, the AMCC data rate can't be too low. We set the AMCC data rate as 24 Mbps to ensure an adequate number of control signal bits in the limited length of the sampling data. On the transmission side, the four-subcarrier signals are generated by DSP in Fig. 5(a) and then sent to arbitrary waveform generator (AWG, M8194A, 120 GSa/s) converting to analog signals. The analog signals are modulated by a dual polarization (DP) I/Q modulator and another input of the modulator is an external cavity laser (ECL) with a wavelength of 1553.6 nm which is used as the signal light source. The modulated signals are amplified by an erbium-doped optical fiber amplifier (EDFA) before being launched into an SMF of 20-km which is a typical access distance for PON. At the receiver side, the optical power of the signal (with AMCC signal) was attenuated by the VOA which emulated the split ratios. As for different values of transmission power, we set different values of VOA to adjust the receiver signal power. Another VOA is used to adjust the LO power. The LO is provided by another ECL with a wavelength of 1553.6 nm. Then, the power-adjusted signal and LO are detected by an integrated coherent receiver (ICR). The detected signals are then captured by an 80 GSa/s digital storage oscilloscope (DSO, UXR0594A, 256 GSa/s with 59 GHz) and demodulated by offline DSP.

The generation steps of transmission signals and the demodulation steps of receiver signals by DSP are shown in Fig. 5(a) and (b), respectively. For the main signal generation steps, the data is first mapped to QPSK for each subcarrier. After that, each subcarrier signal is up-sampled by an up-sampling number of 16 and filtered by a Nyquist pulse-shaping filter with a roll-off factor of 0.1 in sequence. The AMCC signal is superimposed to the main shaped QPSK signal by the multiplication method mentioned in the second section. The superimposed signal with AMCC signal is converted to an analog signal by the AWG. Fig. 5(c) shows the time domain waveform of the received AMCC signal after smooth filtering. Fig. 5(d) shows the spectrum of the superimposed signal with the main signal and AMCC signal. Since the magnitude frequency response of the system is not flattened, the power of low-frequency sub-bands is higher than that of the high-frequency sub-bands. To ensure that each user has a consistent channel resource base and receives a similar signal power, power pre-allocation is used for the four sub-bands.

For receiver-side DSP, each subcarrier is processed independently. Firstly, the receiver signal of each subcarrier is down-sampled and down-converted from −15 GHz, −5 GHz, 5 GHz, and 15 GHz. Then the AMCC signal is detected from the received superimposed signal, and the AMCC signal is demodulated. The main signal is compensated by the generalized signal orthogonalization and projection (GSOP), CDC, and clock recovery. After that, the main signal is recovered by the channel blind equalization algorithm, CMA, FOE, CPE, and DD-LMS. Finally, the main signal is sent to QPSK to demodulate and calculate the BER.

When detecting and demodulating the AMCC signal, the absolute value of the receiver signal is taken to obtain the positive signal. After absolute rectification, the rectified signal is smoothed to smooth time-domain waveforms. Then the signal is energy detected by integration during its period and finally decided according to a specific threshold of its mean value.

V. Experimental Results

In this section, to verify the feasibility of the multiplication scheme superimposed AMCC signal in coherent FDM-PON,

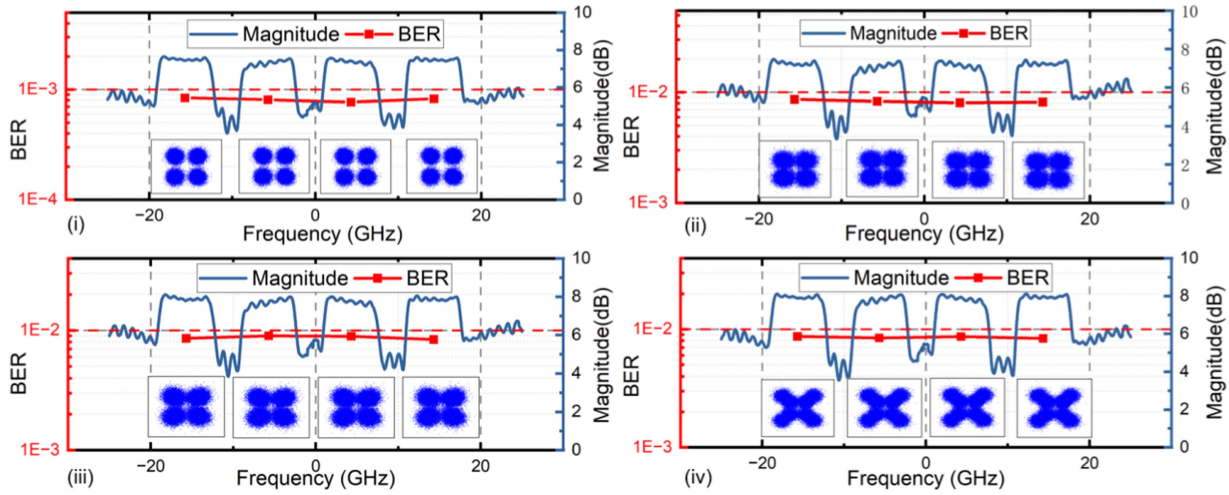

Fig. 8. Spectrum and constellation of the QPSK signal (i) MI = 10.53% @1E-3 (ii) MI = 10.53% @1E-2 (iii) MI = 28.57% @1E-2 (iv) MI = 66.67% @1E-2.

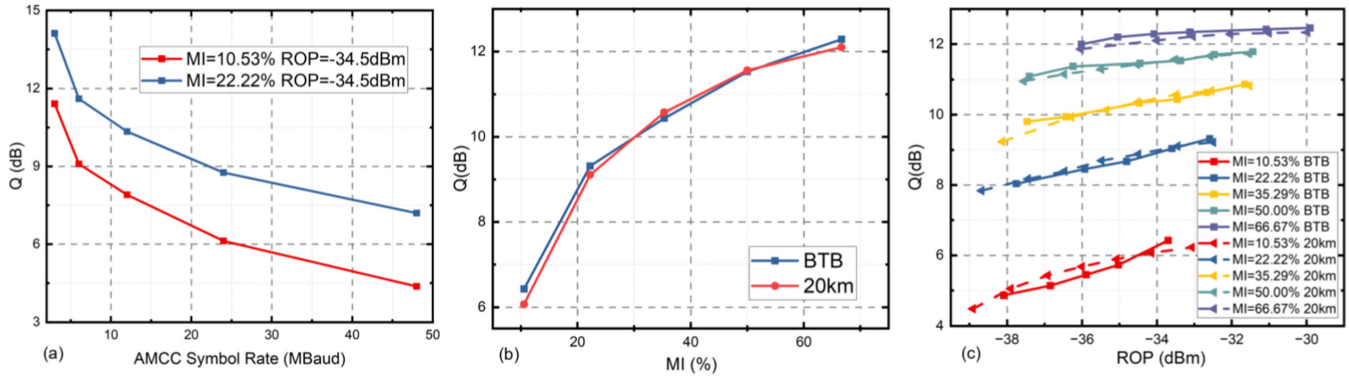

Fig. 9. Results of (a) the NRZ Q versus ROP; (b) the NRZ Q versus MI; (c) the NRZ Q versus AMCC symbol rate.

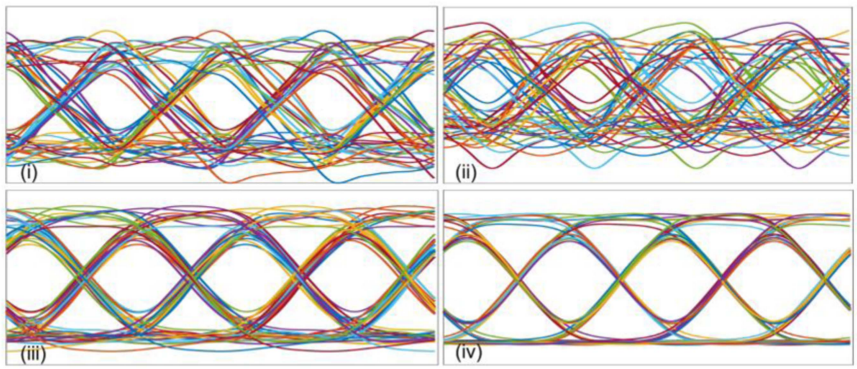

Fig. 10. Eye diagrams of NRZ signals (i) MI = 10.53% @1E-3 (ii) MI = 10.53% @1E-2 (iii) MI = 28.57% @1E-2 (iv) MI = 66.67% @1E-2.

we initially test the performance of the main (QPSK) signal with different MI. We select different amplitudes of AMCC from small to large under several validation scenarios to research the influence of different MIs on the performance of the main signal, these values have universality. Fig. 6(a) shows the calculated BER versus ROP with different MI under BTB, in all tests we notice −37.4 dBm and −34.4 dBm ROP for QPSK signal without AMCC signal at the threshold of 1E-2 and 1E-3. And as the value of MI is larger, the value of ROP is higher under the same threshold. We discover the ROP of the QPSK signal with 10.53% MI is nearly −36.9 dBm at the threshold of 1E−2 and −34 dBm at the threshold of 1E-3. There is nearly 0.5 dB and 0.4 dB D-value between 0 and 10.53% MI at the threshold of 1E-2 and 1E-3. We found the worst situation when MI is 66.67%, the ROP of the QPSK signal is −34.6 dBm and −30.9 dBm, respectively. For this case, we found there is about

2.8 dB and 3.5 dB between 0 and 66.67% MI at the threshold of 1E-2 and 1E-3, respectively. The calculated BER versus ROP with different MI under 20-km SMF transmission is shown in Fig. 6(b). We notice there is a slight difference between the QPSK signal under BTB and 20-km SMF, and the performance of the QPSK signal under 20-km SMF transmission is a little worse than under BTB. In this situation, we notice −37.3 dBm and −34.3 dBm ROP for QPSK signal without AMCC signal at the threshold of 1E-2 and 1E-3. And as the value of MI is larger, the trend is the same as the situation under BTB. And the performance is also the worst when the MI is 66.67%. We found when the QPSK with 66.67% MI, the ROP of the QPSK signal is −34.3 dBm and −30.5 dBm, respectively. There is nearly 3 dB and 3.8 dB D-value between 0 and 66.67% MI at the threshold of 1E-2 and 1E-3. In Fig. 6(a) and (b), (i), (ii), (iii) are constellation chart with 0, 22.22% and 50.00% MI under BTB and 20-km SMF, respectively. From these constellations insets, we can find the performance of QPSK signal is worse as the MI value becomes larger. Comparing to the simulation results, under the same MI value, the experimental results exhibit lower sensitivity. This is attributed to the fact the simulation system is more ideal without bandwidth limitations and quantization noise.

Fig. 7 shows the penalty of the QPSK signal versus MI under different situations. As the values of MI become larger, the penalty of the QPSK signal between two different MI becomes higher. At the threshold of 1E-2, there is nearly the same under BTB and 20-km SMF transmission when the QPSK MI is the same. However, at the threshold of 1E-3, there is still a little difference between BTB and 20-km SMF transmission when the MI of the QPSK signal is the same and the difference is higher as the MI is larger.

When we consider the most extreme case, that is, four subcarriers transmit QPSK signals, the result is shown in Fig. 8(iv). Under a BER threshold of 1E-2, when the value of QPSK signal MI is 66.67%, we found that the constellation in the case is with the worst performance. Other more general situations are shown in (i), (ii) and (iii) of Fig. 8. We can see the value of MI affects the performance of the QPSK signal. As the value of MI increases and the BER threshold decreases, the constellation of the QPSK signal becomes blurry, and performance deteriorates.

For AMCC signal, in order to research the performance of the AMCC signal, we test the value of NRZ signal Q in different cases. Since the AMCC symbol rate impacts the performance of the AMCC signal, we test the Q versus AMCC symbol rate when MI is 10.53% and 22.22%. In Fig. 9(a), the value of Q becomes smaller as the AMCC signal rate grows. Q is the quality factor of the signal, the value of Q is larger, and the performance of the AMCC signal is better. Fig. 9(b) shows the calculated Q versus MI under BTB and 20-km SMF transmission. The value of Q is larger with the MI increasing both under BTB and 20-km SMF transmission. And the value of Q under BTB is basically consistent with the value under 20-km SMF transmission. The calculated Q versus ROP with several MI under BTB transmission and 20-km SMF transmission is shown in Fig. 9(c). The performance is much better as the value of ROP becomes larger. And there is a slight difference of Q between BTB and 20-km SMF. The AMCC signal under BTB and 20-km SMF perform best with 66.67% MI, and the Q value is nearly 12dB when the ROP is −36 dBm. However, when the value of MI is 10.53%, the AMCC signal under BTB and 20-km SMF both perform worst, and the value of Q is nearly 5.5 dB when the ROP is −36 dBm. In the simulation system, the Q factor of the AMCC signal is higher, indicating superior performance of the AMCC signal.

Fig. 10 shows the signal eye diagram of the AMCC signal under different cases when (i) MI = 10.53% @1E-3, (ii) MI = 10.53% @1E-2, (iii) MI = 28.57% @1E-2, (iv) MI = 66.67% @1E-2. In the eye diagram, the height of the eye-opening indicates the value of Q. Obviously, the performance under 66.67% MI is better than that under 10.53% MI. So we notice that MI and BER threshold both affect the performance of the AMCC signal. With the value MI increasing the performance of the AMCC signal becomes better, and with the BER threshold increasing the performance of the AMCC signal becomes worse.

VI. Conclusion

In this work, we utilize AMCC to transmit control information in the coherent FDM-PON. AMCC transmits control information through envelope modulation in the time domain, avoiding additional time slots and bandwidth, which reduces the system latency. In this paper, we propose a novel extraction algorithm for detecting AMCC signals. The receiver DSP blocks for the AMCC signal and the main signal are in two separate branches. We use smooth filtering and energy detection to determine NRZ symbols and extract the AMCC signal from the main signal. And we use the VPIphotonics Design Suite simulation system to verify the feasibility of the proposed scheme for coherent FDM-PON system and explore the minimum symbol rate for AMCC. Finally, we demonstrate a 4-band coherent FDM QPSK PON system with a total data rate of 100 Gbps in the case of carrying a 24 Mbps NRZ-AMCC signal. AMCC can serve as a promising solution for low-latency coherent FDM-PON systems.

References

[1] D. van Veen and V. Houtsma, "Strategies for economical next-generation 50G and 100G passive optical networks [Invited]," *J. Opt. Commun. Netw.*, vol. 12, no. 1, pp. A95–A103, Jan. 2020, doi: 10.1364/JOCN.12.000A95.

[2] J. Zhang, Z. Jia, H. Zhang, M. Xu, J. Zhu, and L. A. Campos, "Rate-flexible single-wavelength TFDM 100G coherent PON based on digital subcarrier multiplexing technology," in *Proc. Opt. Fiber Commun. Conf. Exhib.*, 2020, pp. 1–3.

[3] J. Zhang, Z. Jia, M. Xu, H. Zhang, and L. Alberto Campos, "Efficient preamble design and digital signal processing in upstream burst-mode detection of 100G TDM coherent-PON," *J. Opt. Commun. Netw.*, vol. 13, no. 2, pp. A135–A143, Feb. 2021, doi: 10.1364/JOCN.402591.

[4] N. Kaneda, A. Mahadevan, V. Houtsma, and D. V. Veen, "Coherent PON: System merit and technical challenges," in *Proc. Opto-Electron. Commun. Conf.*, 2021, pp. 1–3, doi: 10.1364/OECC.2021.W2B.1.

[5] N. Suzuki, H. Miura, K. Matsuda, R. Matsumoto, and K. Motoshima, "100 Gb/s to 1 Tb/s based coherent passive optical network technology," *J. Lightw. Technol.*, vol. 36, no. 8, pp. 1485–1491, Apr. 2018, doi: 10.1109/JLT.2017.2785341.

[6] M. S. Faruk, X. Li, D. Nesset, I. N. Cano, A. Rafel, and S. J. Savory, "Coherent passive optical networks: Why, when, and how," *IEEE Commun. Mag.*, vol. 59, no. 12, pp. 112–117, Dec. 2021, doi: 10.1109/MCOM.010.2100503.

[7] A. Shahpari et al., "Coherent access: A review," *J. Lightw. Technol.*, vol. 35, no. 4, pp. 1050–1058, Feb. 2017, doi: 10.1109/JLT.2016.2623793.

[8] H. H. Lee et al., "Demonstration of high-power budget TDM-PON system with 50 Gb/s PAM4 and saturated SOA," *J. Lightw. Technol.*, vol. 39, no. 9, pp. 2762–2768, May 2021, doi: 10.1109/JLT.2021.3059902.

[9] J. S. Wey and J. Zhang, "Passive optical networks for 5G transport: Technology and standards," *J. Lightw. Technol.*, vol. 37, no. 12, pp. 2830–2837, Jun. 2019, doi: 10.1109/JLT.2018.2856828.

[10] P. C. Schindler et al., "Flexible WDM-PON with Nyquist-FDM and 31.25 Gbit/s per wavelength channel using colorless, low-speed ONUs," in *Proc. Opt. Fiber Commun. Conf. Expo. Nat. Fiber Optic Engineers Conf.*, 2013, pp. 1–3, doi: 10.1364/OFC.2013.OW1A.5.

[11] J. Zhang, G. Li, S. Xing, and N. Chi, "Flexible and adaptive coherent PON for next-generation optical access network," *Opt. Fiber Technol.*, vol. 75, 2023, Art. no. 103190.

[12] A. Gatto, P. Parolari, M. Brunero, P. Martelli, R. Brenot, and P. Boffi, "RSOA-based FDM PON upstream with flexible multiple access capabilities in an NG-PON2 compliant architecture," *J. Opt. Commun. Netw.*, vol. 8, no. 5, pp. 302–307, May 2016, doi: 10.1364/JOCN.8.000302.

[13] A. Lebreton et al., "Low complexity FDM/FDMA approach for future PON," in *Proc. Opt. Fiber Commun. Conf. Expo. Nat. Fiber Optic Engineers Conf.*, 2013, pp. 1–3.

[14] *40-Gigabit-Capable Passive Optical Networks (NG-PON2): transmission Convergence Layer Specification*, Standard ITU-T G.989.3, ITU, Geneva, Switzerland, May 2021.

[15] *Gigabit-Capable Passive Optical Networks (G-PON): transmission Convergence Layer Specification*, Standard ITU-T G.984.3, ITU, Geneva, Switzerland, Jan. 2014.

[16] *40-Gigabit-Capable Passive Optical Networks (NG-PON2): transmission Convergence Layer Specification*, Standard ITU-T G.989, ITU, Geneva, Switzerland, Oct. 2015.

[17] K. Honda et al., "Wavelength-shifted protection for WDM-PON with AMCC scheme for 5G mobile fronthaul," in *Proc. Opt. Fiber Commun. Conf. Exhib.*, 2019, pp. 1–3.

[18] C. Wagner et al., "Impairment analysis of WDM-PON based on low-cost tunable lasers," *J. Lightw. Technol.*, vol. 34, no. 22, pp. 5300–5307, Nov. 2016, doi: 10.1109/JLT.2016.2617118.

[19] K. Honda et al., "Wavelength control method of upstream signals using AMCC in WDM-PON for 5G mobile fronthaul," *Opt. Exp.*, vol. 27, no. 19, pp. 26749–26756, 2019.

[20] K. Honda et al., "WDM-PON management and control by auxiliary management and control channel for 5G mobile fronthaul," *Opt. Exp.*, vol. 29, no. 26, pp. 42457–42470, 2021.

[21] H. Guo, C. Yang, X. Qin, Y. Gao, Z. Zheng, and H. Li, "Up to 20 Mb/s auxiliary management and control channel signal transmission in 50 Gb/s PON system," in *Proc. Opt. Fiber Commun. Conf. Exhib.*, 2021, pp. 1–3.

[22] S.-R. Mun, J.-H. Moon, S.-M. Oh, and C.-H. Lee, "A self wavelength tracking method for a cost effective WDM-PON with tunable lasers," in *Proc. Conf. Opt. Fiber Commun., Collocated Nat. Fiber Optic Engineers Conf.*, 2010, pp. 1–3.

[23] K. Honda et al., "Wavelength adjustment of upstream signal using AMCC with power monitoring for WDM-PON in 5G mobile era," in *Proc. Opt. Fiber Commun. Conf. Expo.*, 2018, pp. 1–3.

[24] Z. Tan et al., "Experimental demonstration for over Mbps baseband-over-modulation AMCC implementation in PtP WDM-PON," in *Proc. Opt. Fiber Commun. Conf. Expo.*, 2018, pp. 1–3.

[25] H. Guo, C. Yang, Y. Gao, and H. Li, " AMCC nonlinear baseband superimposition and extraction aided by proposed interference cancellation for WDM-PON used in 5G mobile fronthaul," *Opt. Exp.*, vol. 30, no. 18, pp. 31602–31613, 2022.

[26] R. Igarashi, R. Koma, K. Hara, J. Kani, and T. Yoshida, "Simultaneous reception of AMCC signals and QPSK signals by a single coherent receiver with DSP," *Opt. Exp.*, vol. 30, no. 26, pp. 48030–48041, 2022.

[27] K. Sone, G. Nakagawa, S. Oda, M. Takizawa, Y. Hirose, and T. Hoshida, "Remote management and control of WDM-PON system for fronthaul in cloud-radio access networks," in *Proc. Eur. Conf. Opt. Commun.*, 2017, pp. 1–3, doi: 10.1109/ECOC.2017.8346182.

[28] Y. Wang, W. Shen, and J. Chen, "Demonstration of auxiliary management and control channel signal transmission for FDM coherent passive optical network," in *Proc. Opto-Electron. Commun. Conf.*, 2023, pp. 1–3, doi: 10.1109/OECC56963.2023.10209775.

[29] G. Li, S. Xing, Z. Li, J. Zhang, and N. Chi, "200-Gb/s/λ coherent TDM-PON with wide dynamic range of >30-dB based on local oscillator power adjustment," in *Proc. Opt. Fiber Commun. Conf. Exhib.*, 2022, pp. 1–3.

[30] S. J. Savory, "Digital filters for coherent optical receivers," *Opt. Exp.*, vol. 16, pp. 804–817, 2008.

[31] J. Yu, Z. Dong, J. Zhang, X. Xiao, H.-C. Chien, and N. Chi, "Generation of coherent and frequency-locked multi-carriers using cascaded phase modulators for 10 Tb/s optical transmission system," *J. Lightw. Technol.*, vol. 30, no. 4, pp. 458–465, Feb. 2012.

[32] A. J. Viterbi and A. M. Viterbi, "Nonlinear estimation of PSK-modulated carrier phase with application to burst digital transmission," *IEEE Trans. Inf. Theory*, vol. 29, no. 4, pp. 543–551, Jul. 1983.

[33] G. Li, S. Xing, J. Jia, Z. Li, J. Zhang, and N. Chi, "Local oscillator power adjustment-based adaptive amplification for coherent TDM-PON with wide dynamic range," *J. Lightw. Technol.*, vol. 41, no. 4, pp. 1240–1249, Feb. 2023.